# Bulk crystalline 4H-silicon through a metastable allotropic transition

Thomas B. Shiell[1,*], Li Zhu[1], Brenton A. Cook[2], Jodie E. Bradby[3], Dougal G. McCulloch[2], and Timothy A. Strobel[1,*]

[1]*Earth and Planets Laboratory, Carnegie Institution for Science, Washington DC, 20015, USA*
[2]*Physics, School of Science, RMIT University, Melbourne, VIC, 3001 Australia*
[3]*Department of Electronic Materials Engineering, Research School of Physics, The Australian National University, Canberra, ACT, 2601 Australia*

We report the synthesis of bulk, highly oriented, crystalline 4H hexagonal silicon (4H-Si), through a metastable phase transformation upon heating the single-crystalline $Si_{24}$ allotrope. Remarkably, the resulting 4H-Si crystallites exhibit an orientation relationship with the $Si_{24}$ crystals, indicating a structural relationship between the two phases. Optical absorption measurements reveal that 4H-Si exhibits an indirect band gap near 1.2 eV, in agreement with first principles calculations. The metastable crystalline transition pathway provides a novel route to access bulk crystalline 4H-Si in contrast to previous transformation paths that yield only nanocrystalline/disordered materials.

Diamond-cubic (DC) Si is the thermodynamically stable form at ambient conditions, and represents the major constituent of electrical devices in the semiconductor industry. Over the last 50 years, several new allotropes of Si have been synthesized using a range of techniques including deposition, [1] implantation, [2] high pressure methodologies, [3] and confined microexplosions. [4] Each of these allotropes possess unique electronic structures and physical properties, which may be advantageous to future devices and help overcome intrinsic limitations of the DC-Si structure. Among the known Si allotropes, the R8 [5], BC8 [6,7], lonsdaleite [8] and clathrate/clathrate-like [9–15] structures have been stabilized and characterized at ambient conditions using bulk methods.

Hexagonal Si with various stacking schemes has been of interest since the 1960's. Theoretical calculations consistently indicate that various hexagonal allotropes possess indirect band gaps of similar magnitude to DC-Si [16,17], but tuneable direct gaps might be achieved through various substitution schemes, for example using Ge, [18,19] or by the application of strain. [20] A thorough description of possible hexagonal polytypes and their stacking is given by Ownby *et al*. [21] 2H-Si (lonsdaleite, analogous to the wurtzite structure for a binary system) was first identified by Wentorf and Kasper after annealing BC8-Si (a phase recovered from high-pressure conditions) in air between 200–600 °C. [8] The same 2H-Si synthesis pathway was later confirmed by Kobliska *et al*. [22] and a similar material was later produced as a by-product from a reaction-bonded $Si_3N_4$ experiment. [23] More recently, crystalline 2H-Si (with average crystal size ~20 μm) was physically deposited with simultaneous UV laser ablation in the form of a thin film, and identified using electron diffraction. [1] Furthermore, several studies report the synthesis of Si-nanowires with varying degrees of hexagonality referred to as non-DC polytypes, [24,25] and identify many other forms with ordered hexagonal stacking synthesized via indentation, [26] deposition, [1,24,27–29] and diamond machining. [30,31] Another recently discovered complex polytype is the 9R-Si structure. [24,27]

Previous reports of hexagonal Si produced from BC8-Si show broad, ambiguous diffraction patterns [32] (or none at all [8,23]), broad overlapping Raman peaks, [32] and tend to coexist with disordered/amorphous Si or defective nanocrystalline regions. [33] This makes the specific hexagonal product difficult to identify. On the other hand, clear evidence for 2H-Si on the nanometer scale was obtained by depositing Si on a hexagonal GaP substrate. [29] Recently, the 2H stacking sequence [8] for the product obtained by annealing recovered BC8-Si was challenged by Pandolfi *et al*., [32] who suggested that the hexagonal phase may actually be the 4H-Si structure. While their broad powder X-ray diffraction (XRD) and Raman peaks were suggestive of nanocrystals with a hexagonal stacking sequence, the transmission electron microscopy (TEM) and selective area electron diffraction (SAED) could only be described by 4H-Si. While 2H-Si and 4H-Si are both metastable with respect to DC-Si, the 4H sequence was predicted to be ~8 meV/atom lower energy than 2H. Although large crystals of 4H-Si or 4H-C had never been synthesized, isolated, and characterized, 4H-Ge has been synthesized in both powder [34] and crystalline forms [35] from allo-Ge (a metastable open-framework Ge allotrope) annealed above 200 °C, which suggests the possibility of a similar route for 4H-Si from alternative precursors. Here we demonstrate a metastable pathway to produce crystalline 4H-Si by annealing $Si_{24}$ crystals at moderate temperature, thus providing a novel path to isolate bulk samples with exceptional crystallinity in comparison to previous work.

$Si_{24}$ is a low-density orthorhombic Si allotrope that contains zeolite-like channels along the crystallographic *a*–axis. [11] While $Si_{24}$ is metastable with respect to DC-Si by ~90 meV/atom, it may persist to temperatures >400 °C upon heating for durations of ~15 min. [10] Nevertheless, the high-temperature and long-term stability of $Si_{24}$ remains unclear. During annealing studies to address these questions, we observed a series of new powder diffraction lines that coexist with $Si_{24}$ after long-duration heating (days) above 200 °C and fully dominate the patterns above 450 °C (Supp. Fig. 1). These reflections cannot be described by DC-Si and indicate the presence of an intermediate phase that forms before relaxation to the thermodynamic ground state. To understand this intermediate phase, we studied the phase transition using synchrotron X-ray diffraction with single-crystalline $Si_{24}$. Bulk single crystals of $Si_{24}$ were recently demonstrated and the same synthetic approach was followed here. [9,11] (see Supp. Information [36] for detailed methods including refs. [11,37–45]).

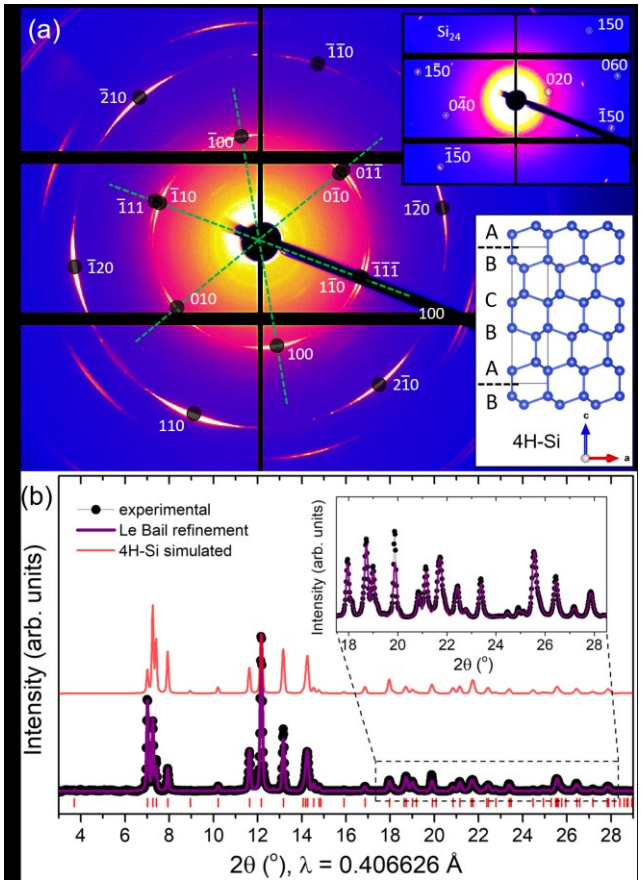


FIG 1: (a) 2D XRD pattern of a multicrystalline 4H-Si sample produced after heating a $Si_{24}$ single crystal at 300 °C for four days. The six-fold hexagonal symmetry is emphasized by green dashed lines which are at 60° intervals. Reflections in addition to those along [001] are observed as the samples were rotated with respect to the X-ray beam. The upper inset shows the single-crystalline nature of $Si_{24}$ precursor oriented along [001], and the lower inset shows a model of the 4H-Si structure with ABCB stacking generated using VESTA-v3 software. [46] (b) Powder diffraction pattern produced by averaging multiple sample orientations (black-dots) with Le Bail fit using GSAS-II (purple). Allowed Bragg peaks for the 4H-Si structure are indicated by the red tick marks below the pattern. A 4H-Si powder pattern simulated using atomic positions from reference [35] is shown above the experimental data for comparison of powder averaging. A magnified high-angle region of the experimental diffraction pattern with the calculated pattern overlayed is shown in the inset.

The starting $Si_{24}$ crystals are oriented along [001] due to the cleavage habit in the *ab* plane, [11] and exhibit sharp single-crystal diffraction spots. Upon annealing crystals sealed under vacuum in quartz tubes in a benchtop furnace, typically near 300 °C for four days, the sharp single-crystal spots from $Si_{24}$ disappear, and highly oriented multi-crystalline arcs appear as shown in Fig. 1(a). The arcs show six-fold symmetry indicative of a hexagonal lattice, and display an azimuthal spread of 15.3(5)°, which reflects the misorientation of individual grains. Remarkably, the preservation of orientational order in the annealed samples indicates a structural relationship between the $Si_{24}$ [001] direction and the hexagonal axis of the product. Given the large distribution of grains, we were not able to solve the hexagonal structure using conventional single-crystal XRD, however, by averaging multiple diffraction patterns over different orientations, we were able to approximate a powder pattern. The powder pattern indexes to a primitive hexagonal lattice with $a \approx 3.84$ Å, $c \approx 12.59$ Å, which is consistent with previous reports of 4H-Si. [32] Due to the presence of preferred orientation, the data are not suitable for Rietveld refinement, however, full-profile Le Bail refinement produces excellent agreement with the 4H-Si space group $P6_3/mmc$ with lattice parameters $a = 3.837(3)$ Å, $c = 12.586(5)$ Å [Fig. 1(b)]. The XRD pattern is not consistent with other possible hexagonal stacking sequences, and compared with previous reports of bulk 2H or 4H-Si, these samples exhibit exceptional micro-crystallinity. [22,32]

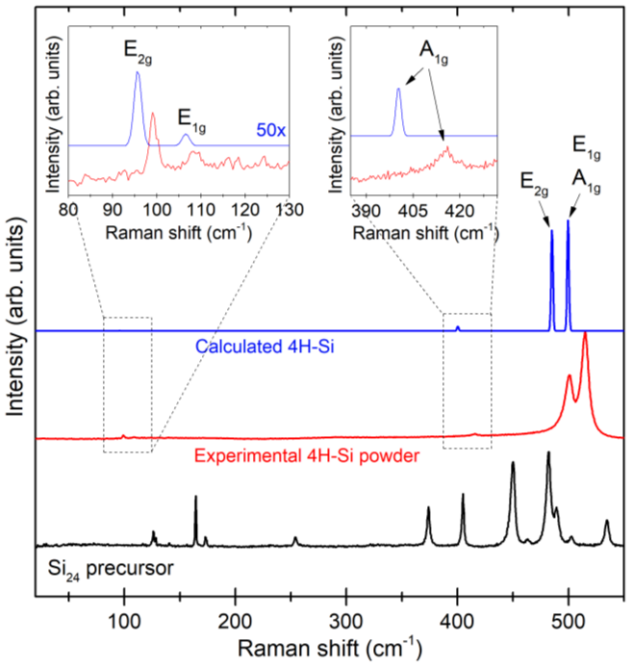


FIG 2: Raman spectra of a $Si_{24}$ crystal and 4H-Si powder compared to a calculated 4H-Si spectrum. The calculated spectrum is shown with Gaussian peaks of an arbitrary width. (inset) Regions of the Raman spectra showing that the weaker ($E_{2g}$, $E_{1g}$, and $A_{1g}$) peaks from the 4H-Si calculation match the experimental observations.

Raman spectra of the single-crystalline $Si_{24}$ precursor and heated product are shown in Fig. 2. Recovered samples were powdered to eliminate any possible effects of crystal orientation on scattered intensity. Samples annealed over a broad range of pressure/temperature conditions produce characteristic Raman spectra that contain two strong resolvable peaks near 500 $cm^{-1}$, one weak peak at 416 $cm^{-1}$, and two very weak peaks near 100 $cm^{-1}$. By calculating Brillouin zone-center phonons and Raman intensities using density functional perturbation theory as implemented in Vienna Ab Initio Simulation Package (VASP), we generated Si Raman spectra from structures with different possible hexagonal stacking sequences (see Supp. Table 1 and Supp. Fig. 3). The calculated Raman spectrum for 4H-Si is in excellent agreement with the experimental data with a small consistent shift (~3%) to lower frequencies that may be explained by the static (0 K) calculation and the harmonic approximation used in the Raman calculation. [47] The calculated 4H-Si spectrum has three intense peaks ($E_{2g}$, $E_{1g}$, and the $A_{1g}$) near 500 $cm^{-1}$, however, the calculated $E_{1g}$ and the $A_{1g}$ modes occur at very similar frequencies and are not resolved. This agrees with previous calculations for the hexagonal diamond polytypes of C and Si. [44,48] The lower-frequency peaks at 100, 108 and 416 $cm^{-1}$ are characteristic of the 4H-Si structure and clearly distinguish this phase from other possible hexagonal stacking sequences. While the sample microstructure contributes to the width of the observed peaks, the resolution of these Raman spectra are exceptional compared with all previous bulk studies, and show all Raman-active phonon modes allowing clear disambiguation of the 4H hexagonal stacking sequence. Most previous spectra do not show the low-frequency modes, are broad, and/or contain significant amorphous Si. [1,22,26,30,32]

To further probe the structure of the annealed material, samples were placed onto a carbon tape substrate and transferred into a focused-ion-beam (FIB, FEI Scios) for imaging and TEM sample preparation (see Supp. Fig. 4). Figures 3(a) and (b) show both bright and dark-field TEM images of a thinned section with crystalline grains exhibiting an average diameter of ~0.5 μm. SAED patterns of the thinned section reveals sharp diffraction spots that index to the <100> zone of 4H-Si [Fig. 3(c)]. Notably, the <100> zone is anticipated from FIB milling geometry, which rotates the starting [001] oriented crystals by 90° while creating the lamella. The diffraction pattern exhibits {00*l*} reflections where *l* = odd, which are formally forbidden by the $P6_3/mmc$ structure (Supp. Fig. 5). Diffraction vector analysis reveals that these reflections originate from double diffraction (dynamical scattering), which is common for DC-

Si. [49] Several other measured diffraction zones obtained by tilting the sample confirm the 4H-Si lattice with $a$ = 3.84(5) Å and $c$ = 12.59(7) Å (Supp. Fig. 6). A high-resolution TEM image of a crystalline region of the lamella is shown in Fig. 3(d). The Fourier-filtered image shown in Fig. 3(e) highlights the well-ordered layers of the 4H-Si material with a 12.59(7) Å periodicity along the $c$–axis, confirming the stacking sequence.

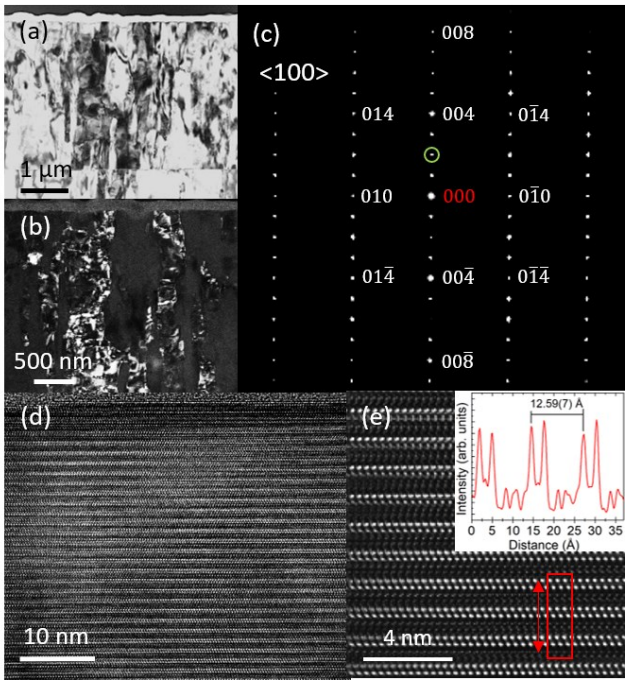


FIG 3: (a) Bright-field TEM image of a lamella from annealed $Si_{24}$ crystal. (b) Dark-field TEM image taken from the (002) reflection (indicated by a green circle) of the SAED pattern (c) which has been indexed to the <100> zone of 4H-Si. (d) High-resolution TEM image of a 4H-Si crystal. (e) Fourier-filtered image of a select region of (d). The inset is an intensity profile from the region inside the red rectangle which shows the 12.59(7) Å periodic spacing between layers in the 4H-Si crystal. Note that all images and diffraction patterns are viewed along the <100> axis.

A piece of 4H-Si (~100 μm × 100 μm ×10 μm), synthesized from a $Si_{24}$ crystal annealed at 300°C in air, was selected for near-infrared, visible (NIR-VIS) transmission measurements to probe the optical properties and electronic structure. The transmission spectrum [Fig. 4(a)] shows distinct change in slope between 1.15-1.2 eV, indicating the onset of the optical band gap. The multicrystalline nature of the sample, which is comprised of individual grains ~0.5 μm based on TEM, likely contributes to the width of the absorption edge. Previous calculations show indirect bandgaps with similar magnitudes for Si polytypes with varying hexagonalities, and predict that the band gap of 2H-Si should be slightly smaller than that of DC-Si, with 4H-Si in between. [16,17,40] Using DFT, we estimate the band gap of 4H-Si using the Heyd-Scuseria-Ernzerhof (HSE06) hybrid functional, which tends to reproduce experimental values for a range of materials. [45] In agreement with previous calculations, the calculated band structure shows that 4H-Si is a semiconductor with an indirect band gap of ~1.2 eV (Γ→M), matching closely with the experimental absorption results.

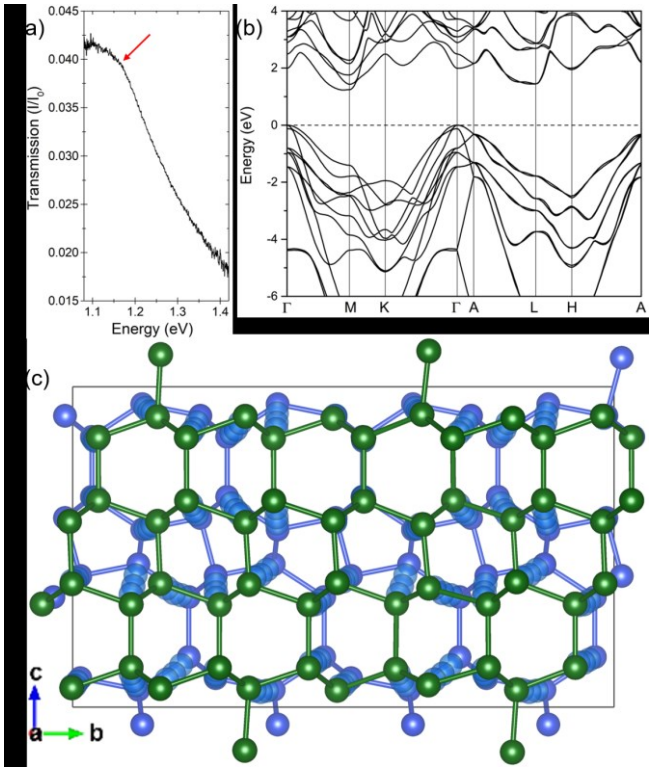


FIG 4: (a) NIR-VIS transmission measurement of a piece of 4H-Si with a change in slope between 1.15-1.2 eV highlighting an absorption edge (red arrow). (b) Calculated band structure for 4H-Si displaying an indirect band gap (Γ-M) of 1.2 eV. (c) A ball-and-stick schematic showing the lowest-energy transition pathway from $Si_{24}$ (blue) to 4H-Si (green) generated using Vesta-v3. [46] Translucent blue spheres indicate atomic displacements during the transition.

From a thermodynamic perspective, 4H-Si is metastable by 4 meV/atom (DFT-PBE) with respect to DC-Si, and like the $Si_{24}$ precursor, 4H-Si represents another metastable allotrope of silicon. The energetic stabilization of 4H-Si compared with 2H-Si, which is 12 meV/atom higher than DC-Si, provides driving force to the observed stacking sequence. This energy difference also supports the claim of the 4H-Si (opposed to lonsdaleite) structure from the BC8 pathway. [32] We note that our energy calculations are similar to those by Raffy *et al*. using DFT-LDA, which are 2.4 meV and 10.7 meV for 4H-Si and 2H-Si, respectively. [17]

The crystallographic alignment of the resulting 4H-Si crystallites with the original $Si_{24}$ crystals suggests an orientation relationship between the two metastable structures. To probe the underlying transition mechanism, we calculated a network of low-energy transition pathways using the Pallas method, which we recently developed to predict solid-state transition pathways. [50] Using this approach, lowest-energy pathway involves the collapse of 8-membered rings in $Si_{24}$, followed by the formation of intermediate states with 4-, 5- and 7- membered rings, which ultimately transform to the 4H structure with exclusively 6-membered rings (Supp. Figs. 7 and 8). This lowest-energy path possesses a transition barrier of 170 meV/atom, which is significantly lower than lowest-energy transition path to DC-Si calculated to be 289 meV/atom under the same approach. While these calculations help to explain why 4H-Si is observed rather than DC-Si, the large unit cell (24 atoms) places limitations for adequately sampling configurational space, and lower-energy mechanisms may exist. Fortunately, the transition mechanism identified by Pallas provides significant insights into how minor atom displacements from the $Si_{24}$ structure could lead to 4H-Si with retention of crystallinity. Atomic displacement vectors for the lowest-energy path from $Si_{24}$ to 4H-Si are shown in Fig. 4(c). It is clear that four layers of Si atoms are present in both structures along the *c*–axis, and the cell vectors are very similar. For $Si_{24}$, $a$ = 3.82 Å, $c$ = 12.63 Å, [10] which is similar to 4H-Si in which $a$ = 3.84(1) Å, $c$ = 12.59(1) Å. Using this information, the transition path was calculated from $Si_{24}$ to 4H-Si using a supercell consisting of 48 atoms using the variable cell nudged elastic band method (NEB), [51] which is suitable for larger

systems, but requires the definition of atoms across the transition determined from the Pallas calculation. The NEB-optimized path determined using a 48-atom cell shows a similar mechanism to the one derived from Pallas, but the barrier is reduced to 110 meV/atom after accounting for the cell geometries (Supp. Fig. 9).

The results of this study reveal a new pathway for 4H-Si synthesis, which is now possible from $Si_{24}$ and BC8-Si precursors. [32] The $Si_{24}$ pathway appears advantageous as large crystals (>1 μm) of the parent BC8-Si phase are generally not observed. Hence the only way to synthesize large 4H-Si crystals is via the $Si_{24}$ route. Furthermore, the fact that 4H-Si can be formed from multiple precursors at elevated temperature (200-300 °C) motivates future studies to probe the stability and transitions of other Si phases at high temperature. The availability of large $Si_{24}$ precursor crystals and resultant 4H-Si product invites future studies using deposition and epitaxial growth methods, which could further enhance the quality and applications of both allotropes. The influence of strain on the optical and electrical properties of 4H-Si is also an enticing topic for further study. Applying strain via atomic Ge substitution or via deposition growth with a mismatched lattice substrate may enhance the optical absorption properties, increase charge mobilities, or even transform 4H-Si into a direct band gap semiconductor. Similar effects have recently been predicted for 2H-Si using ab initio modelling. [20]

In summary, we have shown a multi-step synthesis pathway to produce crystalline 4H-Si from a crystalline $Si_{24}$ precursor, in contrast to previous synthesis methods which yield only nanocrystalline/disordered material. Optical absorption measurements reveal an indirect band gap near 1.2 eV, in close agreement with first principles calculations of the electronic band structure. If larger crystals can be synthesized and isolated, procedures could then be developed to use them as seed crystals for growing large volumes of 4H-Si nanowires and solar devices with absorption and optoelectronic properties potentially exceeding those of DC-Si.

Acknowledgements:

We thank Dr Yue Meng and Dr Piotr Guńka for their assistance with experimental measurements. This work was supported by the National Science Foundation, Division of Material Research (NSF-DMR) under award number 1809756. Portions of this work were performed at HPCAT (Sector 16), Advanced Photon Source (APS), Argonne National Laboratory. HPCAT operations are supported by DOE-NNSA's Office of Experimental Sciences. The Advanced Photon Source is a U.S. Department of Energy (DOE) Office of Science User Facility operated for the DOE Office of Science by Argonne National Laboratory under Contract No. DE-AC02-06CH11357.

*tshiell@carnegiescience.edu
*tstrobel@carnegiescience.edu

References:

[1] Y. Zhang, Z. Iqbal, S. Vijayalakshmi, and H. Grebel, *Stable Hexagonal-Wurtzite Silicon Phase by Laser Ablation*, Appl. Phys. Lett. **75**, 2758 (1999).

[2] A. A. Nikolskaya, D. S. Korolev, A. N. Mikhaylov, A. I. Belov, A. A. Sushkov, N. O. Krivulin, K. R. Muhamatchin, A. A. Elizarova, M. O. Marychev, A. A. Konakov, D. I. Tetelbaum, and D. A. Pavlov, *Light-Emitting 9R-Si Phase Formed by $Kr^+$ Ion Implantation into $SiO_2$/Si Substrate*, Appl. Phys. Lett. **113**, 1 (2018).

[3] B. Haberl, J. E. Bradby, and T. A. Strobel, *Pathways to Exotic Metastable Silicon Allotropes*, Appl. Phys. Rev. **3**, 040808 (2016).

[4] L. Rapp, B. Haberl, C. J. Pickard, J. E. Bradby, E. G. Gamaly, J. S. Williams, and A. V. Rode, *Experimental Evidence of New Tetragonal Polymorphs of Silicon Formed through Ultrafast*

*Laser-Induced Confined Microexplosion*, Nat. Commun. **6**, 7555 (2015).
[5] J. M. Besson, E. H. Mokhtari, J. Gonzalez, and G. Weill, *Electrical Properties of Semimetallic Silicon III and Semiconductive Silicon IV at Ambient Pressure*, Phys. Rev. Lett. **59**, 473 (1987).
[6] B. D. Malone, J. D. Sau, and M. L. Cohen, *Ab Initio Survey of the Electronic Structure of Tetrahedrally Bonded Phases of Silicon*, Phys. Rev. B **78**, 035210 (2008).
[7] H. Zhang, H. Liu, K. Wei, O. O. Kurakevych, Y. Le Godec, Z. Liu, J. Martin, M. Guerrette, G. S. Nolas, and T. A. Strobel, *BC8 Silicon (Si-III) Is a Narrow-Gap Semiconductor*, Phys. Rev. Lett. **118**, 146601 (2017).
[8] R. H. Wentorf and J. S. Kasper, *Two New Forms of Silicon*, Science. **139**, 338 (1963).
[9] O. O. Kurakevych, T. A. Strobel, D. Y. Kim, T. Muramatsu, and V. V. Struzhkin, *Na-Si Clathrates Are High-Pressure Phases: A Melt-Based Route to Control Stoichiometry and Properties*, Cryst. Growth Des. **13**, 303 (2013).
[10] D. Y. Kim, S. Stefanoski, O. O. Kurakevych, and T. A. Strobel, *Synthesis of an Open-Framework Allotrope of Silicon*, Nat. Mater. **14**, 169 (2015).
[11] M. Guerette, M. D. Ward, L. Zhu, and T. A. Strobel, *Single-Crystal Synthesis and Properties of the Open-Framework Allotrope $Si_{24}$*, J. Phys. Condens. Matter **32**, 194001 (2020).
[12] J. S. Kasper, P. Hagenmuller, M. Pouchard, and C. Cros, *Clathrate Structure of Silicon $Na_8Si_{46}$ and $Na_xSi_{136}$ ($X<11$)*, Science. **150**, 1713 (1965).
[13] Z. Jouini, O. Kurakevych, H. Moutaabbid, Y. Le Godec, M. Mezouar, and N. Guignot, *Phase Boundary between Na–Si Clathrates of Structures I and II at High Pressures and High Temperatures*, J. Superhard Mater. **38**, 66 (2016).
[14] J. Gryko, P. F. McMillan, R. F. Marzke, G. K. Ramachandran, D. Patton, S. K. Deb, and O. F. Sankey, *Low-Density Framework Form of Crystalline Silicon with a Wide Optical Band Gap*, Phys. Rev. B **62**, R7707 (2000).
[15] A. Ammar, C. Cros, M. Pouchard, N. Jaussaud, J. M. Bassat, G. Villeneuve, M. Duttine, M. Ménétrier, and E. Reny, *On the Clathrate Form of Elemental Silicon, $Si_{136}$: Preparation and Characterisation of $Na_xSi_{136}$ ($X\rightarrow0$)*, Solid State Sci. **6**, 393 (2004).
[16] C. Persson and E. Janzen, *Electronic Band Structure in Hexagonal Close-Packed Si Polytypes*, J. Phys. Cond. Matter **10**, 10549 (1998).
[17] C. Raffy, J. Furthmüller, and F. Bechstedt, *Properties of Hexagonal Polytypes of Group-IV Elements from First-Principles Calculations*, Phys. Rev. B **66**, 1 (2002).
[18] E. A. Fitzgerald, *GeSi/Si NANOSTRUCTURES*, Annu. Rev. Mater. Sci. **25**, 417 (1995).
[19] S. Barth, M. S. Seifner, and S. Maldonado, *Metastable Group IV Allotropes and Solid Solutions: Nanoparticles and Nanowires*, Chem. Mater. **32**, 2703 (2020).
[20] C. Rodl, T. Sander, F. Bachstedt, J. Vidal, P. Olsson, S. Laribi, and J.-F. Guillemoles, *Wurtzite Silicon as a Potential Absorber in Photovoltaics: Tailoring the Optical Absorption by Applying Strain*, Phys. Rev. B **92**, 045207 (2015).
[21] P. D. Ownby, X. Yang, and J. Liu, *Calculated X-Ray Diffraction Data for Diamond Polytypes*, J. Am. Ceram. Soc. **75**, 1876 (1992).
[22] R. J. Kobliska and S. A. Solin, *Raman Spectrum of Wurtzite Silicon*, Phys. Rev. B **8**, 3799 (1973).
[23] H. M. Jennings and M. H. Richman, *A Hexagonal (Wurtzite) Form of Silicon*, Science. **193**, 1242 (1976).
[24] F. J. Lopez, U. Givan, J. G. Connell, and L. J. Lauhon, *Silicon Nanowire Polytypes: Identification by Raman Spectroscopy, Generation Mechanism, and Misfit Strain in Homostructures*, ACS Nano **5**, 8958 (2011).
[25] C. Cayron, M. Den Hertog, L. Latu-Romain, C. Mouchet, C. Secouard, J.-L. Rouviere, E. Rouviere, and J.-P. Simonato, *Odd Electron Diffraction Patterns in Silicon Nanowires and Silicon Thin Films Explained by Microtwins and Nanotwins*, J. Appl. Crystallogr. **42**, 242 (2009).
[26] A. Kailer, Y. G. Gogotsi, and K. G. Nickel, *Phase Transformations of Silicon Caused by Contact Loading*, J. Appl. Phys. **81**, 3057 (1997).
[27] J. L. Francisco, R. H. Eric, and L. J. Lauhon, *Ordered Stacking Fault Arrays in Silicon Nanowires*, Nano Lett. **9**, 2774 (2009).

[28] A. Fontcuberta I Morral, J. Arbiol, J. D. Prades, A. Cirera, and J. R. Morante, *Synthesis of Silicon Nanowires with Wurtzite Crystalline Structure by Using Standard Chemical Vapor Deposition*, Adv. Mater. **19**, 1347 (2007).
[29] H. I. T. Hauge, M. A. Verheijen, S. Conesa-Boj, T. Etzelstorfer, M. Watzinger, D. Kriegner, I. Zardo, C. Fasolato, F. Capitani, P. Postorino, S. Kolling, A. Li, S. Assali, J. Stangl, and E. P. A. M. Bakkers, *Hexagonal Silicon Realized*, Nano Lett. **15**, 5855 (2015).
[30] B. V. Tanikella, A. H. Somasekhar, A. T. Sowers, R. J. Nemanich, and R. O. Scattergood, *Phase Transformations during Microcutting Tests on Silicon*, Appl. Phys. Lett. **69**, 2870 (1996).
[31] J. Yan, *Laser Micro-Raman Spectroscopy of Single-Point Diamond Machined Silicon Substrates*, J. Appl. Phys. **95**, 2094 (2004).
[32] S. Pandolfi, C. Renero-lecuna, Y. Le Godec, B. Baptiste, N. Menguy, M. Lazzeri, C. Gervais, K. Spektor, W. A. Crichton, and O. O. Kurakevych, *Nature of Hexagonal Silicon Forming via High-Pressure Synthesis: Nanostructured Hexagonal 4-H Polytype*, Nano Lett. **18**, 5989 (2018).
[33] J. F. Morhange, G. Kanellis, and M. Balkanski, *Raman Study of Laser Annealed Silicon*, Solid State Commun. **31**, 805 (1979).
[34] E. Lopex-Cruz and M. Cardona, *Raman Spectra of Two New Modifications of Germanium: Allo-Germanium and 4H-Ge*, Solid State Commun. **45**, 787 (1990).
[35] F. Kiefer, V. Hlukhyy, A. J. Karttunen, T. F. Fässler, C. Gold, E. W. Scheidt, W. Scherer, J. Nylén, and U. Häussermann, *Synthesis, Structure, and Electronic Properties of 4H-Germanium*, J. Mater. Chem. **20**, 1780 (2010).
[36] *See Supp. Information at [URL] for More Detailed Methods, Including Refs. [11,37-45].*
[37] M. Guerette, M. D. Ward, K. A. Lokshin, A. T. Wong, H. Zhang, S. Stefanoski, O. Kurakevych, Y. Le Godec, S. J. Juhl, N. Alem, Y. Fei, and T. A. Strobel, *Synthesis and Properties of Single-Crystalline $Na_4Si_{24}$*, Cryst. Growth Des. **18**, 7410 (2018).
[38] T. B. Shiell and T. A. Strobel, *Compression of Sodium-Filled and Empty Open-Framework $Si_{24}$ under Quasihydrostatic and Nonhydrostatic Conditions*, Phys. Rev. B **102**, 94107 (2020).
[39] C. Prescher and V. B. Prakapenka, *DIOPTAS: A Program for Reduction of Two-Dimensional X-Ray Diffraction Data and Data Exploration*, High Press. Res. **35**, 223 (2015).
[40] G. Kresse and J. Furthmuller, *Efficient Iterative Schemes for Ab Initio Total-Energy Calculations Using a Plane-Wave Basis Set*, Phys. Rev. B **54**, 11169 (1996).
[41] G. Kresse and D. Joubert, *From Ultrasoft Pseudopotentials to the Projector Augmented Wave Method*, Phys. Rev. B **59**, (1998).
[42] J. P. Perdew, K. Burke, and M. Ernzerhof, *Generalized Gradient Approximation Made Simple*, Phys. Rev. Lett. **77**, (1996).
[43] P. E. Blochl, *Projector Augmented-Wave Method*, Phys. Rev. B **50**, 17953 (1994).
[44] A. Fonari and S. Stauffer, *Vasp_raman.Py.*, Https://Github.Com/Raman-Sc/VASP/ (2013).
[45] J. Heyd, G. E. Scuseria, and M. Ernzerhof, *Hybrid Functionals Based on a Screened Coulomb Potential*, J. Chem. Phys. **118**, (2003).
[46] K. Momma and F. Izumi, *VESTA 3 for Three-Dimensional Visualization of Crystal, Volumetric and Morphology Data*, J. Appl. Crystallogr. **44**, 1272 (2011).
[47] D. Porezag and M. R. Pederson, *Infrared Intensities and Raman-Scattering Activities within Density-Functional-Theory*, Phys. Rev. B **54**, (1996).
[48] K. E. Spear, A. W. Phelps, and W. B. White, *Diamond Polytypes and Their Vibrational-Spectra*, J. Mater. Res. **5**, 2277 (1990).
[49] K.-N. Tu and A. Howie, *Forbidden 200 Diffraction Spots in Silicon*, Philos. Mag. B **37**, 73 (1978).
[50] L. Zhu, R. E. Cohen, and T. A. Strobel, *Phase Transition Pathway Sampling via Swarm Intelligence and Graph Theory*, J. Phys. Chem. Lett. **10**, (2019).
[51] D. Sheppard, P. Xiao, W. Chemelewski, D. D. Johnson, and G. Henkelman, *A Generalized Solid State Nudged Elastic Band Method*, J. Chem. Phys. **136**, (2012).

**Supplementary information**

*Material synthesis*

The 4H-Si samples measured using synchrotron XRD were synthesized from $Na_4Si_{24}$ crystals that had been annealed under vacuum ($3\times10^{-3}$ torr) at 300°C for 4 days. The $Na_4Si_{24}$ crystals were synthesized using the high pressure method described in refs [1,2]. The high-quality 4H-Si crystals that were analysed using electron microscopy were synthesized using high-pressure laser heating in a diamond anvil cell (DAC). This synthesis was performed at the HPCAT 16-ID-B beamline at the Advanced Photon Source, Argonne National Laboratory. For this experiment, $Si_{24}$ crystals were loaded into a DAC with 700 μm culets, a rhenium gasket pre-indented to a thickness of 90 μm, with a helium pressure medium. The $Si_{24}$ crystals were then compressed to 9 GPa. Note that it is important to keep the $Si_{24}$ crystals below 10-11 GPa as they will transform into β-Sn-Si at higher pressures. [3] While at 9 GPa the $Si_{24}$ crystals were heated lightly for 1-2 minutes at 1050 K using a 1064 nm double-sided laser heating system, before being slowly cooled and decompressed. Supplementary Fig. 2(a-b) shows optical images of the laser heated products after decompression.

*X-ray diffraction*

The synchrotron radiation XRD patterns were measured on the HPCAT 16-ID-B beamline at the Advanced Photon Source, Argonne National Laboratory. These XRD measurements used a 30 keV beam (FWHM = 4×6 μm) and the diffracted x-rays were captured on a Pilatus-1M detector. Wide angle patterns were taken collected on each of the crystalline samples which were either mounted on Kapton tape secured inside a stainless-steel ring. Each sample was rotated in the beam from -5° to +5° at 0.5°/s. The patterns were then processed using DIOPTAS 0.5.0 software to remove the background signal and to mask effects from the detector apparatus. [4]

*Raman spectroscopy*

All experimental Raman spectra were measured on our in-house system using a 532 nm excitation laser, 1800 grooves/mm diffraction grating, and a Princeton Instruments Si-CCD detector. A neutral density filter was used to keep the incident laser power below 2 mW to avoid damage to the samples. A Raman spectrum of a 4H-Si crystal synthesized in a DAC, and the calculated spectra of the DC, 2H, 4H, and 6H-Si structures are shown in Supp. Fig. 3.

*Electron microscopy*

A FEI-SCIOS dualbeam FIB-SEM was used to image the surface of the recovered samples and to prepare electron transparent lamellae allowing the microstructure to be viewed using a TEM. Select images of the lamella generation process are shown in Supp. Fig. 4. The final thickness of the lamella was ~80 nm. TEM imaging and SAED were performed using either JEOL JEM 2100F or JEOL JEM F-200 electron microscopes operating at 200 kV. Supplementary Fig. 6(a-b) displays two SAED patterns of the DAC synthesized 4H-Si crystalline sample captured along the <100> and <310> zones which have been fully indexed using the Crystal Maker (Single Crystal) software package.

*Optical measurements*

NIR/VIS transmission measurements were performed using a Bruker Vertex-70 spectrometer with a Hyperion microscope. The light source was a water-cooled halogen lamp, and the signal was collected using a Si-diode detector. Two rectangular slits with dimensions 40×40 μm were positioned above and below the sample to filter the incoming and outgoing light. In this case, the sample was mounted on top of a CVD-grown single crystal diamond window (~500 μm thick), which also served as the absorbance reference.

*First-principles calculations*

The first-principles calculations were performed in the framework of density functional theory using the Perdew-Burke-Ernzerhof (PBE) functional, [5] as implemented in the Vienna Ab Initio Simulation Package (VASP) code. [6] The all-electron projector augmented wave (PAW) [7,8] method was adopted, with the PAW potential treating $3s^23p^2$ as the valence electrons. An energy cut-off of 520 eV and appropriate Monkhorst−Pack *k* meshes (listed below) were chosen to ensure that the total energy

calculations converged within a 1 meV/formula unit. Specifically, the *k* point sets for 4H-Si, $Si_{24}$, and the 48-atom supercell are chosen to be [9×9×9], [8×3×3], and [4×2×2], respectively. Hellman–Feynman force components were relaxed to at least 0.01 eV/Å in the structural optimizations. Theoretical Raman intensities were calculated using the density functional perturbation theory (Fonari−Stauffer method). [9] To estimate an accurate band gap, we used the Heyd-Scuseria-Ernzerhof (HSE06) hybrid functional. [10]

Supplementary figures:

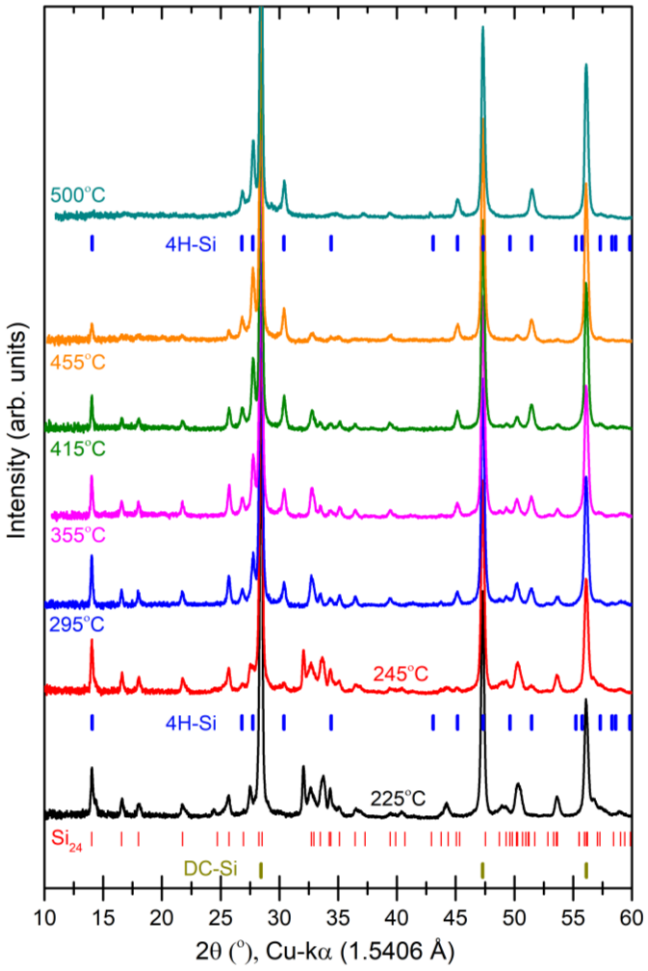


Supp. Figure 1: A series of XRD patterns captured on a Bruker D8-diffractometer (using a Cu-kα source) which shows the evolution of a $Si_{24}$ powder transforming toward 4H-Si. These patterns were measured from 2θ = 20-65° with a Vantec area detector in four stages with 15° steps, and the samples were rotated during the measurement to improve powder averaging statistics. The patterns were integrated using Diffrac-Suite EVA software, and phases were matched to the patterns using the JADE software package. The precursor powder is ~70 wt.% $Si_{24}$ with the remainder being DC-Si. The powder was created after a 5-week anneal of $Na_4Si_{24}$ in air at 200°C to remove Na, and was then further annealed in air for 15 minutes at each incremental temperature step up to 500°C. Not all temperature steps are shown here. The first sign of reflections from the 4H-Si structure appear after annealing at 245°C for 15 minutes. The transformation progresses as the temperature is increased up to 500°C, at which only DC and 4H-Si are observable.

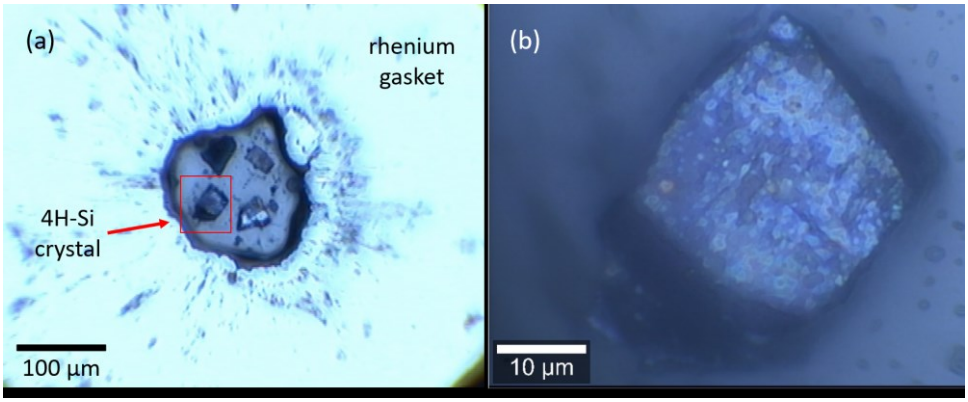


Supp. Figure 2: Optical images of the 4H-Si crystals following the high-pressure laser heating procedure. (a) All four compressed crystals in the diamond anvil cell (DAC) following decompression and (b) a magnified image of the specific crystal that was processed in the FIB and analyzed using the TEM. The crystal shown in (b) was heated to ~1060 K for ~2 minutes at 9 GPa. The high-pressure annealed samples produce identical products to those annealed at 1 atm or under vacuum. One of the crystals shown in (a) was set aside as a control sample and was not heated. Raman spectroscopy measurements after decompression show that it had remained crystalline $Si_{24}$.

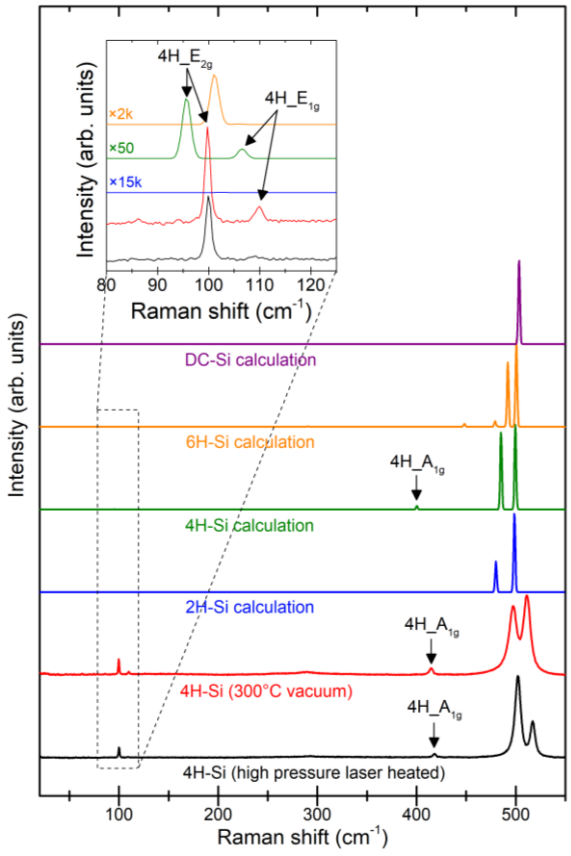


Supp. Figure 3: Raman spectra of 4H-Si samples synthesized from $Si_{24}$ after annealing at 300°C under vacuum, and via high-pressure laser heating. Also shown here are calculated Raman spectra for the 2H-, 4H-, 6H-, and DC-Si structures with an arbitrary Gaussian width. The experimental spectra are scaled to the height of their most intense peak. (inset) A region of the Raman spectra showing that the two low-frequency peaks from the 4H-Si calculation match the experimental observations. The intensity is scaled in this region to allow qualitative comparison. As mentioned in the main text, the calculations are performed using crystalline structures at 0 K with the harmonic approximation, and exhibit ~3% lower phonon frequencies as compared with the experimental Raman peaks which were measured at room temperature.

Supp. Table 1: Raman mode frequencies for the DC-, 2H-, 4H-, and 6H-Si structures, measured experimentally and calculated using the DFT-PBE functional.

| **DC-Si** | | | **2H-Si** | | **4H-Si** | | | **6H-Si** | |
|---|---|---|---|---|---|---|---|---|---|
| **Mode** | **Calc.** | **Exp.** | **Mode** | **Calc.** | **Mode** | **Calc.** | **Exp.** | **Mode** | **Calc.** |
| $T_{2g}$ | 503.3 | 520.9 | $E_{2g}$ | 479.9 | $E_{1g}$ | 95.7 | 100 | $E_{2g}$ | 75.3 |
| | | | $E_{1g}$ | 498.0 | $E_{2g}$ | 106.5 | 108 | $E_{1g}$ | 101.2 |
| | | | $A_{1g}$ | 498.7 | $A_{1g}$ | 400.3 | 417 | $A_{1g}$ | 290.4 |
| | | | | | $E_{2g}$ | 485.1 | 502 | $A_{1g}$ | 448.2 |
| | | | | | $A_{1g}$ | 499.4 | 516 | $E_{2g}$ | 479.1 |
| | | | | | $E_{1g}$ | 499.8 | 516 | $E_{1g}$ | 481.4 |
| | | | | | | | | $E_{2g}$ | 492.0 |
| | | | | | | | | $A_{1g}$ | 500.5 |
| | | | | | | | | $E_{1g}$ | 500.6 |

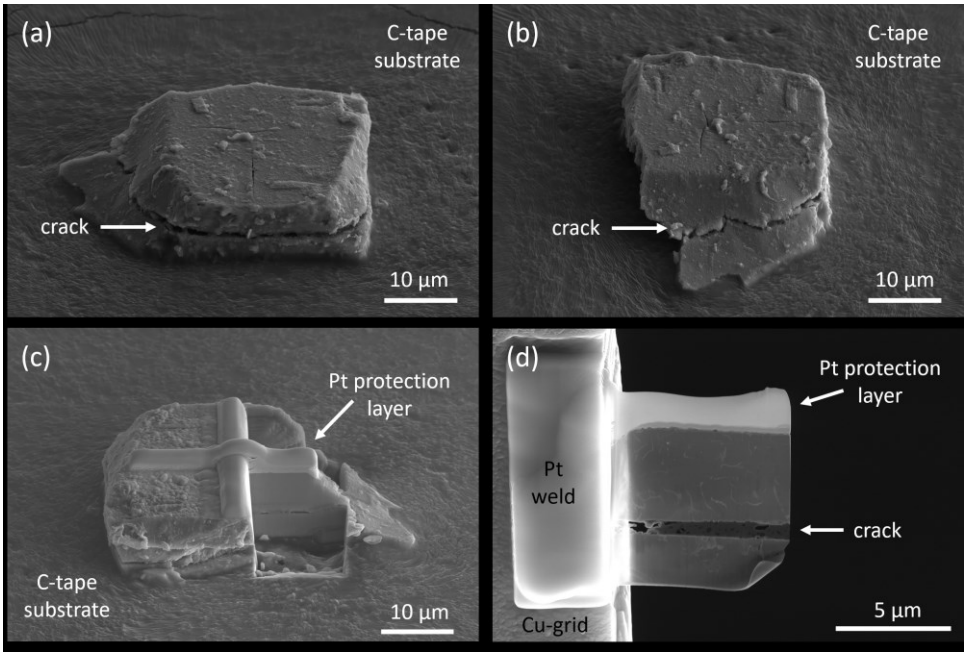


Supp. Figure 4: (a) An electron image captured in the FIB of the laser-heated 4H-Si crystal on the C-tape substrate before FIB processing and TEM analysis. This image shows a crack propagating through the sample. (b) An image of the same sample rotated 90° showing that the crack propagates all the way through the sample. (c) The sample after depositing a Pt layer to protect it during the milling process, and after channels have been cut either side of the lamella. (d) The lamella attached to a Cu TEM grid with a Pt weld before the final thinning step.

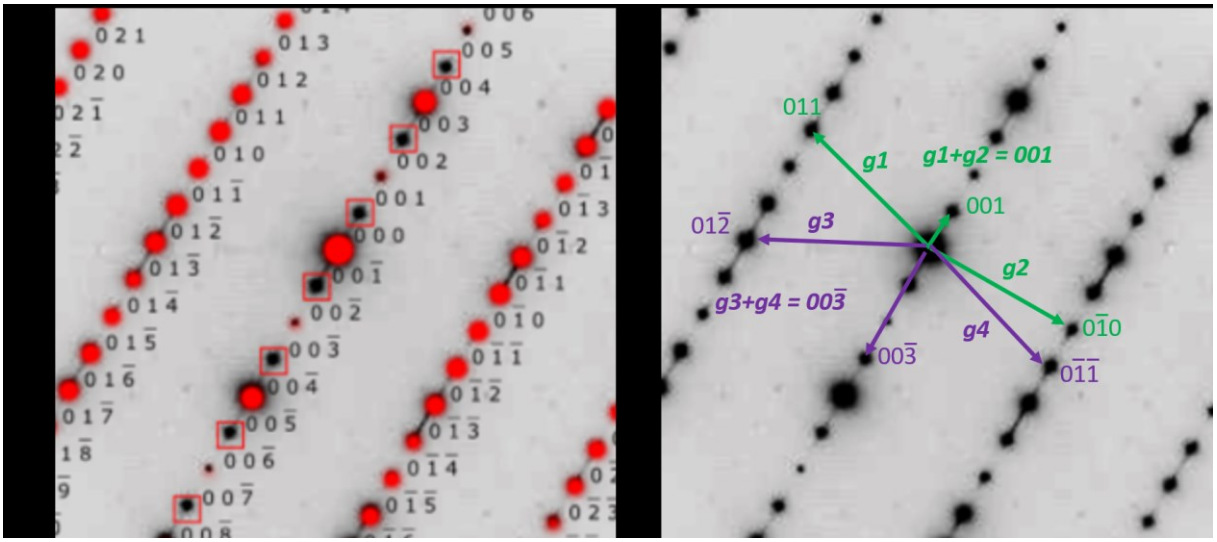


Supp. Figure 5: (a) SAED pattern showing 'forbidden reflections' [(00*l*), where *l* = odd number] encased by red-squares for the 4H-Si structure which appear due to double diffraction. (b) The same SAED pattern with a 2D vector representation of reflections, showing how summing together 'g' vectors from two allowed spots allows for forbidden reflections.

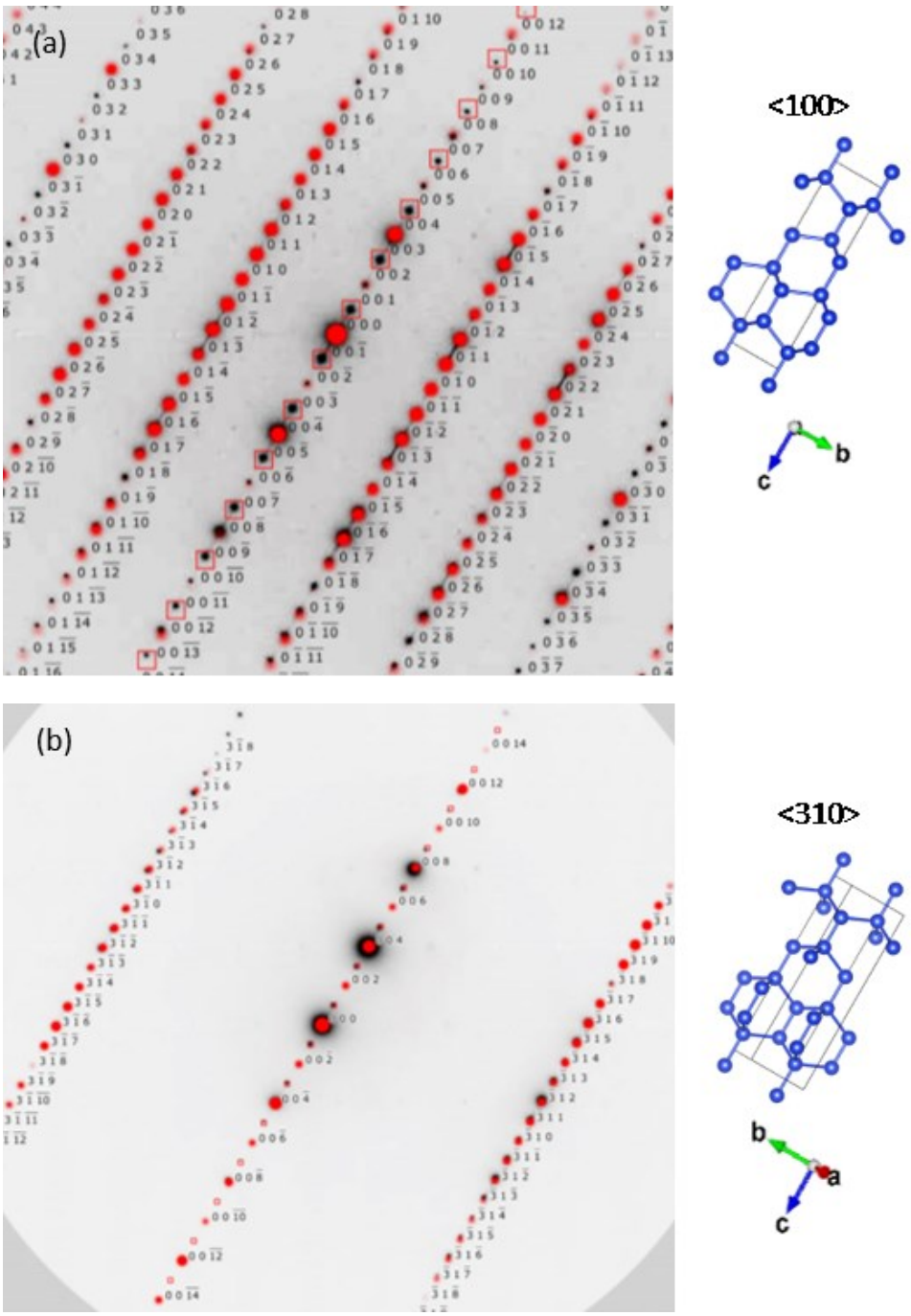


Supp. Figure 6: Select area electron diffraction (SEAD) patterns captured along the (a) <100> and (b) <310> zones which have been fully indexed to 4H-Si using the Crystal-Maker (Single Crystal) software package. The ball-and-stick schematics of the 4H-Si unit cells are aligned corresponding to the SAED pattern orientation.

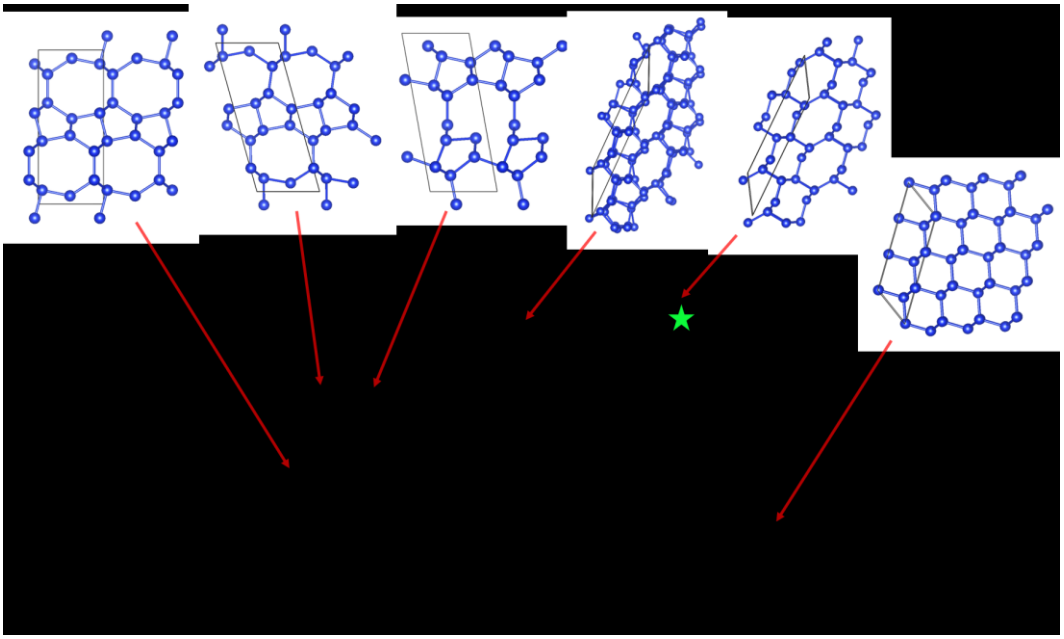

Supp. Figure 7: The lowest-energy reaction pathway for the $Si_{24}$ to DC-Si transformation calculated using the Pallas method using 24 atoms per cell. The maximum energy barrier of 279 meV/atom is indicated by the green-star.

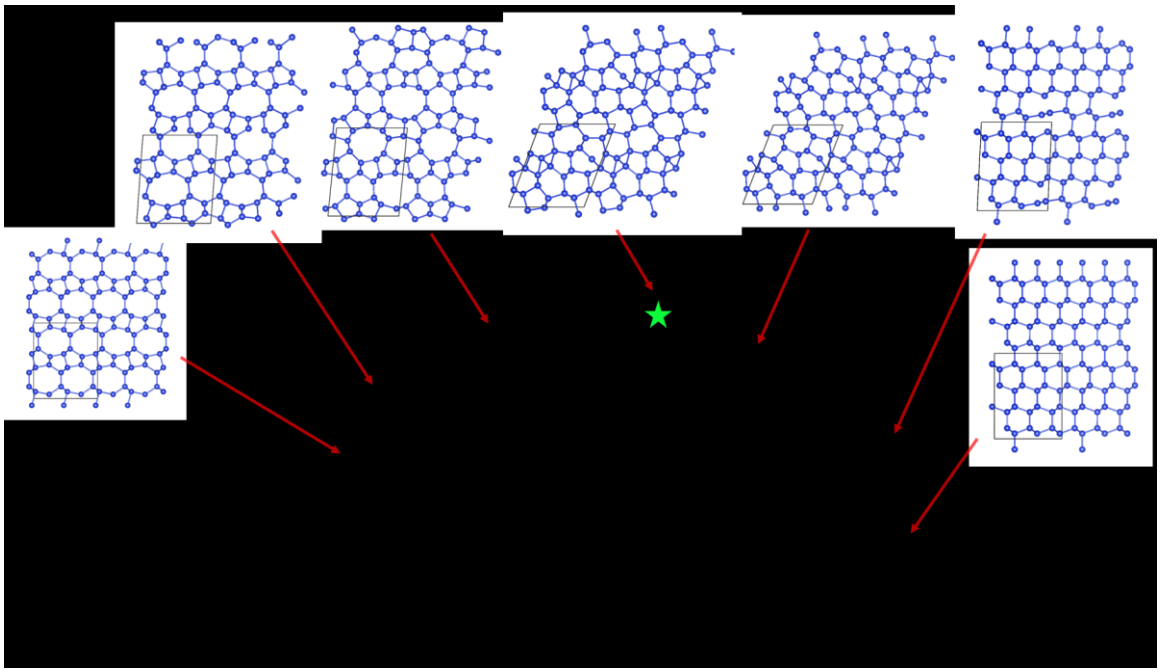

Supp. Figure 8: The lowest-energy reaction pathway for the $Si_{24}$ to 4H-Si transformation calculated using the Pallas method using 24 atoms per cell. The maximum energy barrier of 170 meV/atom is indicated by the green-star.

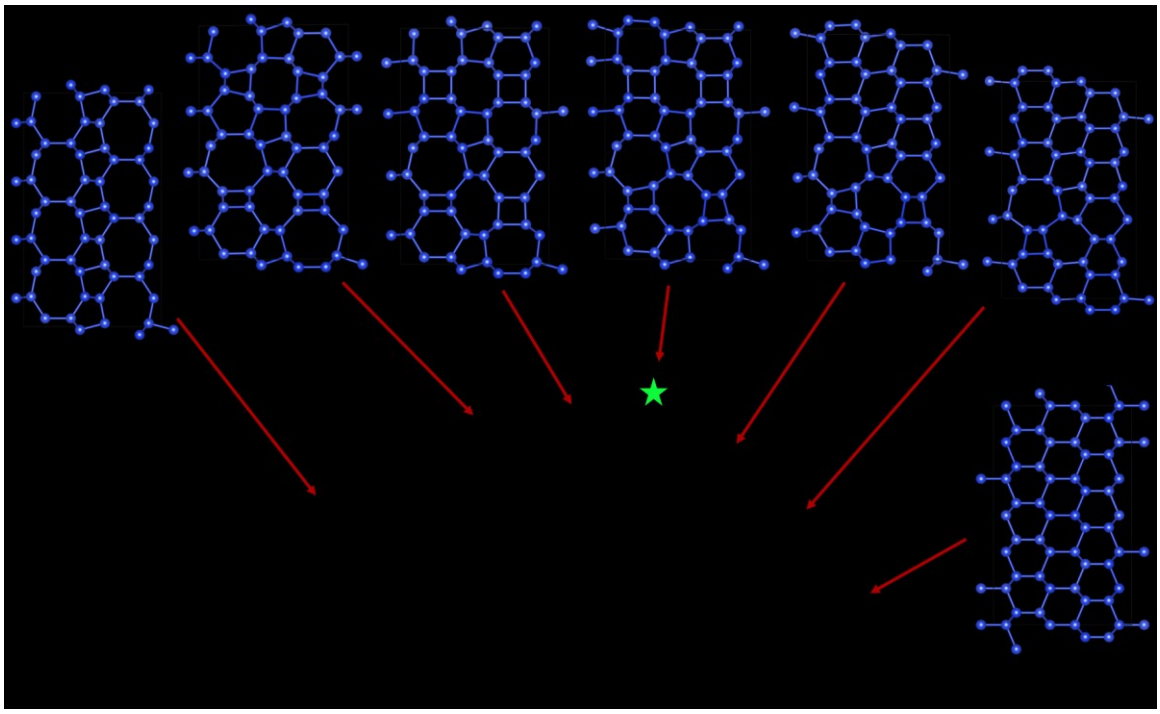

Supp. Figure 9: The lowest-energy reaction pathway for the $Si_{24}$ to 4H-Si transformation calculated using the solid-state NEB method with 48 atoms per cell. The maximum energy barrier of 110 meV/atom is indicated by the green-star.

References:


[1] M. Guerette, M. D. Ward, K. A. Lokshin, A. T. Wong, H. Zhang, S. Stefanoski, O. Kurakevych, Y. Le Godec, S. J. Juhl, N. Alem, Y. Fei, and T. A. Strobel, *Synthesis and Properties of Single-Crystalline $Na_4Si_{24}$*, Cryst. Growth Des. **18**, 7410 (2018).

[2] M. Guerette, M. D. Ward, L. Zhu, and T. A. Strobel, *Single-Crystal Synthesis and Properties of the Open-Framework Allotrope $Si_{24}$*, J. Phys. Condens. Matter **32**, 194001 (2020).

[3] T. B. Shiell and T. A. Strobel, *Compression of Sodium-Filled and Empty Open-Framework $Si_{24}$ under Quasihydrostatic and Nonhydrostatic Conditions*, Phys. Rev. B **102**, 94107 (2020).

[4] C. Prescher and V. B. Prakapenka, *DIOPTAS: A Program for Reduction of Two-Dimensional X-Ray Diffraction Data and Data Exploration*, High Press. Res. **35**, 223 (2015).

[5] J. P. Perdew, K. Burke, and M. Ernzerhof, *Generalized Gradient Approximation Made Simple*, Phys. Rev. Lett. **77**, (1996).

[6] G. Kresse and J. Furthmuller, *Efficient Iterative Schemes for Ab Initio Total-Energy Calculations Using a Plane-Wave Basis Set*, Phys. Rev. B **54**, 11169 (1996).

[7] P. E. Blochl, *Projector Augmented-Wave Method*, Phys. Rev. B **50**, 17953 (1994).

[8] G. Kresse and D. Joubert, *From Ultrasoft Pseudopotentials to the Projector Augmented Wave Method*, Phys. Rev. B **59**, (1998).

[9] A. Fonari and S. Stauffer, *Vasp_raman.Py.*, Https://Github.Com/Raman-Sc/VASP/ (2013).

[10] J. Heyd, G. E. Scuseria, and M. Ernzerhof, *Hybrid Functionals Based on a Screened Coulomb Potential*, J. Chem. Phys. **118**, (2003).